

Detection of new sources of methanol emission at 95 GHz with the Mopra telescope

I.E. Val'tts,¹ S.P. Ellingsen,² V.I. Slysh,¹ S.V. Kalenskii,¹
R. Otrupcek³ and G.M. Larionov¹

¹*Astro Space Center of Lebedev Physical Institute, Profsoyuznaya 84/32, 117810 Moscow, Russia*

²*School of Mathematics and Physics, University of Tasmania, GPO Box 252-21, Hobart 7001, TAS, Australia*

³*Australia Telescope National Facility, PO Box 76, Epping 2121, NSW, Australia*

Received date; accepted date

ABSTRACT

A southern hemisphere survey of methanol emission sources has been carried out using the ATNF Mopra millimetre telescope. 85 sources, the majority of them masers, have been detected in the $8_0 - 7_1 A^+$ transition of methanol at 95 GHz. Together with a similar northern hemisphere survey this completes the search for 95-GHz methanol emission from the Galactic Plane. The previously found correlation between intensity of methanol emission at 44 and 95 GHz is confirmed here with the larger sample of sources. The results of LVG statistical equilibrium calculations confirm the classification of these sources as class I methanol masers pumped through collisional excitation.

Key words: ISM: radio lines: ISM – masers – surveys – ISM: molecules

1 INTRODUCTION

Methanol, OH and H₂O masers are all frequently associated with massive star formation regions, however, methanol masers offer more possibilities for the study of star forming regions than either OH or H₂O, because there are numerous transitions in the microwave region of spectrum. One of the most widespread methanol masers is the $7_0 - 6_1 A^+$ transition at 44 GHz. About 50 masers from this transition have been detected in the northern hemisphere (Morimoto, Ohishi & Kanzawa 1985, Haschick, Menten & Baan 1990, Bachiller et al. 1990, Kalenskii et al. 1992, Kalenskii et al. 1994) and a similar number have been found in the southern hemisphere (Slysh et al. 1994). According to the empirical scheme of Menten (1991), the 44 GHz $7_0 - 6_1 A^+$ transition is a class I methanol maser. Class I methanol masers differ from class II methanol masers in that they are not directly associated with compact HII regions and OH masers, and the two classes also emit in different transitions.

The $8_0 - 7_1 A^+$ transition at 95 GHz is an analogue of the 44-GHz maser transition (see Fig. 1 of Val'tts et al. (1999)). The upper (8_0) energy level of the 95-GHz transition is 18.5K higher than the upper (7_0) energy level of the 44-GHz transition and modelling (Cragg et al. 1992) shows that strong maser emission is also expected from this transition. Val'tts et al. (1995) carried out a search for 95-GHz methanol masers with the Onsala radiotelescope which detected a large number, mostly at the position of 44-GHz

masers and with spectra similar to the spectra of the 44-GHz masers. The intensity of 95-GHz masers was found to correlate with intensity of 44-GHz masers, and was on average about 0.5 of the intensity 44-GHz masers. In this paper we present the results of the first search for 95-GHz methanol masers in the southern hemisphere, carried out with the ATNF Mopra telescope in Australia. This search completes a whole sky survey of class I methanol masers source in two transitions, at 44 and 95 GHz.

2 OBSERVATIONS

The observations were carried out in the period from July 1 to 17, 1997, using the Mopra 22-m millimeter-wave telescope of the ATNF. The assumed rest frequency of the $8_0 - 7_1 A^+$ transition of methanol was 95.169489 GHz (De Lucia et al. 1989). At this frequency only the inner 15 metres of the Mopra antenna is illuminated and the aperture efficiency is 41%, which implies that one Kelvin of antenna temperature corresponds to 40 Jy. The half-power beamwidth of the Mopra antenna at 95 GHz is 52''. The observations were performed in a position switching mode with reference positions offset 30' in declination. The antenna pointing was checked and corrected every 12 hours by making observations of 86-GHz SiO masers, the nominal pointing accuracy when this procedure is followed is 10'' rms. For the majority of sources observations were only made at the nominal

position, as time limitations did not permit the observation of grids at offset positions (to accurately determine the position) to be made. A grid of observations were observed toward a number of interesting sources, and for some cases where the 95-GHz emission was anomalously low. A number of these grids found the strongest emission to be offset from the nominal position and in some cases this will be due to antenna pointing errors. However, many of the sources have only been observed in lower frequency class I transitions and the offset may be due to limited accuracy to which the source position has been previously determined.

A cryogenically cooled low-noise SIS mixer was used in the receiver. The single side-band receiver noise temperature was 110 K and the system temperature varied between 220 K and 320 K depending on weather conditions and the elevation of the telescope. An ambient temperature load (assumed to have a temperature of 290 K) was regularly placed in front of the receiver to enable calibration using the method of Kutner & Ulich (1981). This corrects the observed flux density for the effects of atmospheric absorption, ohmic losses and rear-ward spillover. Variations in the ambient temperature of a few percent occurred during the observations, and the estimated uncertainty of the absolute flux density scale is 10%.

For the majority of the observations the back-end was a 64 MHz wide 1024-channel autocorrelator with a frequency resolution of 62.5 kHz. This yields a velocity resolution at 95 GHz of 0.236 km s^{-1} with uniform weighting and 0.394 km s^{-1} with Hanning smoothing. Some sources were reobserved with the correlator configured to a 32 MHz bandwidth, also with 1024 spectral channels. This yields a velocity resolution of 0.118 km s^{-1} with uniform weighting and 0.197 km s^{-1} with Hanning smoothing. For each source a uniformly weighted spectrum was produced with a velocity width of approximately 80 km s^{-1} centred on the velocity of the previously detected class I or II methanol maser emission. The spectrum was then Hanning smoothed to improve the signal-to-noise ratio of weak sources. For the Mopra observations, the spectra in all figures and Gaussian parameters (peak flux density, velocity and full width half maximum) in all tables are Hanning smoothed data collected with the 64-MHz correlator configuration, unless otherwise noted in Table 1.

The source list was compiled primarily from 44-GHz class I methanol masers detected in the southern hemisphere by Slysh et al. (1994) and Haschick et al. (1990). The observing list also included 12 class I methanol masers detected at 36 GHz at Puschino (Kalenskii, private communication), 55 class II methanol sources which had not previously been searched for class I maser emission (Caswell et al. 1995, Ellingsen et al. 1996, Ellingsen et al. 1999, Walsh et al. 1997) and 12 HII regions for which no 44-GHz emission was detected by Slysh et al. (1994).

3 RESULTS

A total 153 sites were searched for 95-GHz methanol emission, with detections observed toward 85. Table 1 contains a list of all detected sources along with the Gaussian parameters of their spectral features. Their spectra are shown in Fig. 1. The sources toward which no 95-GHz emission was

detected are listed in Table 2, along with the $3-\sigma$ limit (typically less than 5 Jy). The kinematic distance to each source was estimated using the rotation curve of Brand & Blitz (1993). For many of the sources the model yields two distance estimates, The majority are likely to be at the nearer distance, but we have not attempted to resolve the ambiguity and where it occurs both distances are listed in Table 1 & 2. 86 known 44- or 36-GHz class I methanol sources were observed, with 95-GHz emission being detected toward 71 (83%). A total of 54 class II methanol maser sites which had not previously been searched for class I methanol emission were also observed, yielding a total of 13 detections (24%).

Seventy nine of the 85 sources in Table 1 are new detections, the other 6 were discovered previously by Val'tts et al. (1995) at Onsala. In Table 3 we compare the Gaussian parameters of the strongest features of 6 sources observed at both Onsala and Mopra. The radial velocities agree within 0.4 km s^{-1} in all cases, which is approximately half the spectral resolution of the Onsala observations. The flux densities agree to within a factor of 2, which is reasonable, taking into account differences in the spectral resolution, absolute calibration and possible pointing errors. Examination of Table 3 shows that some of the masers (e.g. OMC-2 and NGC2264) have very narrow lines of 0.2 km s^{-1} , which were completely unresolved with the 0.7 km s^{-1} spectral resolution of the Onsala observations. The Onsala results have not been corrected for spectral smoothing, and for this reason, very narrow features in OMC-2, NGC2264 and W51Met2 will have lower peak flux density than that observed at Mopra. Below we give comments for some of the more interesting sources.

3.1 Comments on individual sources

OMC-2. The 95-GHz methanol maser in this source consists of a very intense narrow line similar to that observed at 44 GHz (Haschick et al. 1990). The peak flux densities at both frequencies are almost equal, as are the line widths.

NGC2264. This source shows an intense narrow line at 95 GHz with a shoulder on the positive velocity side. The spectrum of the 95-GHz methanol maser is very similar to that at 44-GHz, but the peak flux density is a factor of two lower.

305.21+0.21. The spectra of the 95- and 44-GHz masers are very similar, showing a single intense narrow line with the 95-GHz flux density only 25% lower than the 44-GHz flux density.

333.13-0.43. The spectrum of this source in Fig.1 shows a weak broad line. Comparing this spectrum with the 44-GHz spectrum we suspected that 95-GHz flux density was too low, possibly because of a pointing error. To check this we made a five-point map consisting of an observations at the central position and offset by $\pm 20''$ in both right ascension and declination. Fig. 2 contains the spectra from this map, which shows that the strongest emission is offset to the south-west of the nominal position and that there are at least two rather strong narrow lines confirming that this is a maser.

333.23-0.05. This source (Fig.1) has an intense isolated spectral feature, which is best fitted by two Gaussians. A five-point map (Fig. 3) shows that the source is in fact offset from the nominal position by approximately $-20''$ in

Table 1. Detected 95-GHz methanol sources. Gaussian parameters were determined from 64 MHz Hanning smoothed spectra, except where noted. a=Gaussian parameters determined from uniformly weighted spectrum; b=Gaussian parameters determined from 32-MHz bandwidth spectrum; c=Detection only marginal. Distances were determined using the Galactic rotation curve model of Brand & Blitz (1993), except where otherwise noted. 1=Genzel & Stutzki (1989); 2=Sung, Bessell & Lee (1997); 3=Neckel (1978); 4=Houghton & Whiteoak (1995); 5=Thronson, Lowenstein & Stokes (1979)

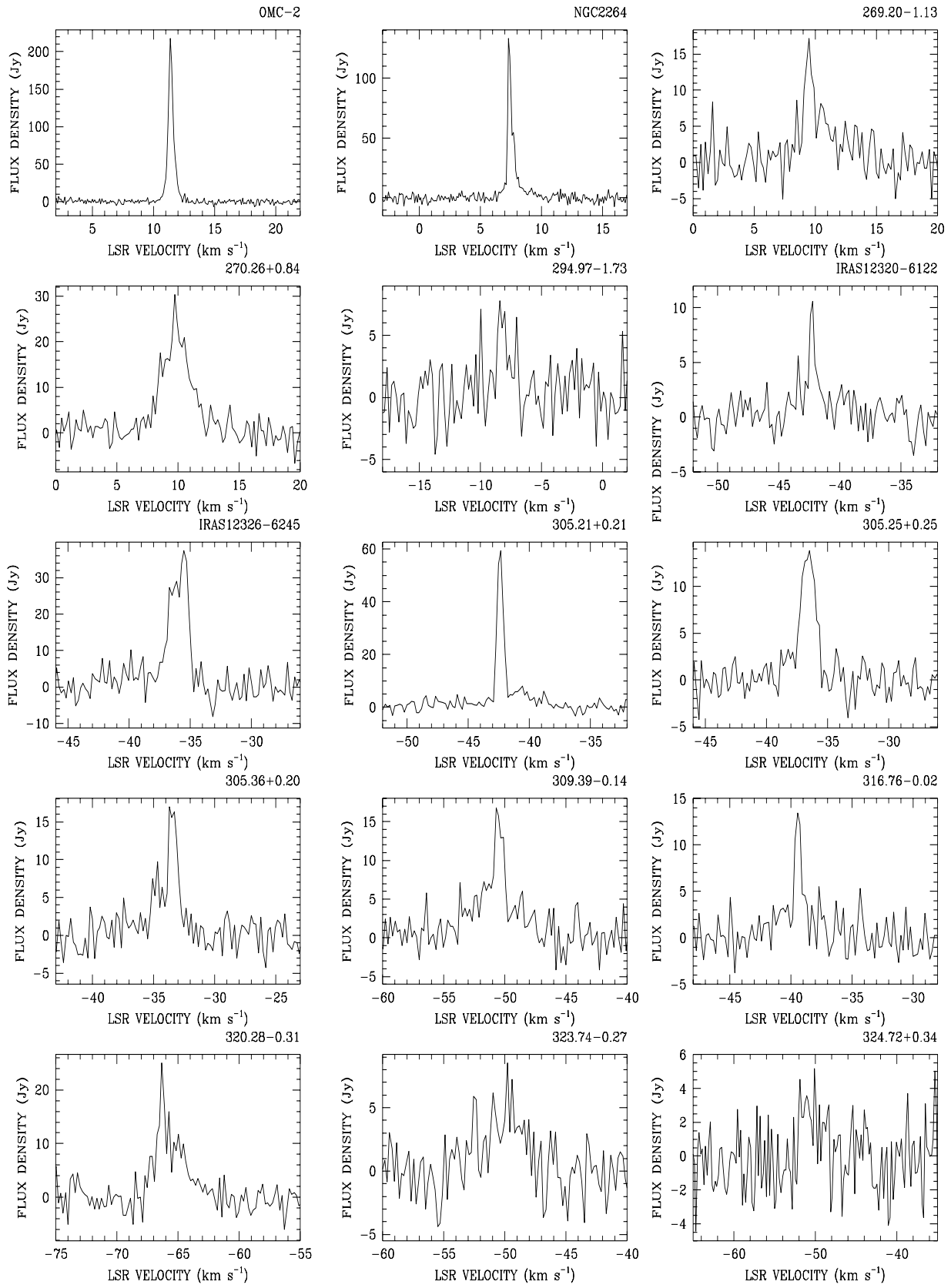
Source	R.A. 1950 (h m s)	Dec. 1950 ($^{\circ}$ $'$ $''$)	Peak Flux Density (Jy)	LSR radial velocity (km s $^{-1}$)	Line FWHM (km s $^{-1}$)	Distance Near (kpc)	Distance Far (kpc)
OMC-2a,b	05:32:59.80	-05:11:29.0	4(2) 138(7) 85(7)	10.9(0.2) 11.4(0.01) 11.5(0.01)	0.9(0.5) 0.3(0.01) 0.7(0.03)	0.45 ¹	
NGC2264a,b	06:38:24.90	09:32:28.0	99.2(5.7) 55.2(3.7)	7.3(0.01) 7.6(0.03)	0.2(0.02) 0.7(0.04)	0.76 ²	
269.20-1.13 ^a	09:01:52.96	-48:16:07.1	15.1(2.3) 6.5(1.5)	9.4(0.1) 10.7(0.2)	0.7(0.1) 1.6(0.6)	2.9	3.2
270.26+0.84 ^a	09:14:56.26	-47:43:34.1	7.0(3.1) 21.0(1.6)	9.3(0.1) 9.8(0.1)	0.6(0.4) 2.8(0.2)	3.1	
294.97-1.73	11:36:51.54	-63:12:09.4	5.9(0.8)	-8.2(0.1)	1.3(0.2)	0.6	6.6
300.97+1.15 ^a	12:32:02.60	-61:23:06.0	9.4(1.2)	-42.2(0.05)	0.7(0.1)	4.2	
301.14-0.23 ^a	12:32:42.60	-62:45:57.0	27.8(2.4) 27.2(8.1)	-36.3(0.2) -35.4(0.05)	1.5(0.3) 0.6(0.1)	4.4	
305.21+0.21 ^{a,b}	13:07:57.54	-62:18:44.2	62.1(2.5)	-42.4(0.01)	0.61(0.03)	4.9	
305.25+0.25 ^a	13:08:20.50	-62:16:07.0	13.9(0.8)	-36.6(0.4)	1.4(0.1)	2.5	7.3
305.36+0.20 ^a	13:09:21.00	-62:17:30.0	7.8(1.4) 17.4(1.4)	-34.8(0.1) -33.4(0.4)	0.9(0.2) 0.9(0.1)	2.8	7.0
309.39-0.14	13:43:55.90	-62:03:14.0	5.6(0.8) 11.0(1.7)	-51.0(0.3) -50.5(0.1)	5.0(0.6) 0.7(0.1)	2.2	8.5
316.76-0.02 ^a	14:41:07.81	-59:35:33.1	12.9(1.6)	-39.4(0.1)	0.7(0.1)	2.7	9.7
320.28-0.31	15:06:25.71	-58:14:02.2	5.3(1.4) 14.5(1.9)	-67.2(0.1) -66.3(0.02)	0.5(0.2) 0.7(0.1)	4.6	8.5
			9.5(0.6)	-65.1(0.2)	2.4(0.3)		
323.74-0.27	15:27:52.41	-56:20:48.1	4.3(1.0) 4.9(0.4)	-52.5(0.1) -49.8(0.1)	0.5(0.1) 2.9(0.3)	3.3	10.4
324.72+0.34	15:31:06.71	-55:17:28.0	3.1(0.5)	-50.6(0.2)	2.5(0.4)	3.4	10.5
326.475+0.703	15:39:27.05	-53:57:42.5	4.4(2.2) 16.0(2.0)	-41.5(0.5) -40.9(0.1)	9.6(1.9) 3.9(0.4)	2.6	11.6
			7.9(1.6)	-40.8(0.1)	0.7(0.2)		
326.641+0.612	15:40:43.44	-53:56:05.9	15.8(0.6)	-39.4(0.1)	4.3(0.2)	2.9	11.3
327.392+0.199	15:46:27.84	-53:48:01.7	5.7(0.5) 3.7(0.6)	-89.4(0.1) -88.3(0.2)	1.1(0.2) 0.8(0.3)	5.3	9.0
326.859-0.667	15:47:20.40	-54:49:03.6	8.9(0.7)	-67.1(0.1)	1.9(0.2)	3.7	10.5
327.618-0.111	15:48:58.76	-53:54:05.4	6.0(0.5)	-88.2(0.04)	1.3(0.1)	6.5	7.9
327.29-0.58	15:49:13.01	-54:28:12.1	9.8(2.3) 14.3(1.1)	-47.2(0.4) -44.6(0.2)	3.0(0.5) 2.5(0.9)	3.0	11.3
			5.1(1.6)	-42.0(0.8)	3.5(1.1)		
328.81+0.64	15:52:00.01	-52:34:03.9	3.6(1.6) 1.2(1.1)	-43.0(0.2) -42.0(0.2)	1.6(0.6) 0.6(0.6)	2.9	11.6
			1.3(0.9)	-41.0(0.2)	0.9(0.7)		
			7.2(0.9)	-40.9(0.3)	3.1(0.4)		
328.24-0.55	15:54:06.12	-53:50:47.1	2.7(0.6) 4.0(0.9)	-44.0(0.2) -42.9(0.1)	1.1(0.5) 0.8(0.3)	2.8	11.6
			7.3(0.4)	-41.2(0.1)	1.8(0.2)		
329.469+0.502	15:55:52.44	-52:14:58.0	3.7(0.7) 4.5(0.6)	-69.5(0.5) -66.7(0.4)	2.4(0.8) 3.1(0.7)	4.5	10.1
			2.3(0.7)	-63.4(0.1)	0.8(0.3)		
329.03-0.21 ^a	15:56:42.01	-53:04:22.1	19.3(1.3) 10.3(3.3)	-43.7(0.1) -42.5(0.1)	1.3(0.1) 0.5(0.2)	3.1	11.4
			12.5(1.6)	-41.7(0.1)	0.9(0.3)		
			9.5(1.5)	-40.5(0.1)	0.9(0.3)		
329.066-0.308	15:57:18.97	-53:07:38.5	2.2(0.4) 2.6(0.9)	-42.2(0.3) -42.0(0.1)	4.3(0.9) 0.5(0.2)	3.0	11.6
			7.0(0.3)	-49.8(0.1)	2.2(0.2)	3.6	11.0
329.183-0.314	15:57:56.13	-53:03:22.4	2.5(0.5)	-47.5(0.2)	1.6(0.4)		

Table 1 – *continued*

Source	R.A. 1950 (h m s)	Dec. 1950 ($^{\circ}$ $'$ $''$)	Peak Flux Density (Jy)	LSR radial velocity (km s $^{-1}$)	Line FWHM (km s $^{-1}$)	Distance Near (kpc)	Distance Far (kpc)
331.13–0.25	16:07:11.01	–51:42:53.1	20.5(0.7) 5.7(0.4) 5.7(0.4)	–91.0(0.02) –88.5(0.2) –84.8(0.2)	1.0(0.04) 2.8(0.5) 3.0(0.4)	5.5	9.4
331.442–0.187	16:08:24.07	–51:27:28.6	4.4(0.6) 3.9(0.6)	–91.5(0.1) –87.9(0.1)	0.4(0.2) 1.1(0.2)	5.4	9.6
331.34–0.35 ^a	16:08:37.41	–51:38:32.1	15.8(1.3)	–65.7(0.03)	0.7(0.1)	4.2	10.7
332.295–0.094	16:11:58.11	–50:48:26.0	4.9(1.9) 3.2(0.6)	–49.6(0.1) –48.8(0.3)	0.6(0.2) 1.2(0.6)	3.2	11.8
332.604–0.167 ^a	16:13:42.20	–50:38:51.4	8.8(0.9)	–45.8(0.04)	0.9(0.1)	3.5	11.6
333.23–0.05 ^a	16:16:02.01	–50:07:50.1	26.3(1.0) 2.9(1.7)	–87.2(0.03) –86.2(0.2)	1.2(0.1) 0.7(0.4)	5.3	9.9
333.13–0.43	16:17:13.01	–50:28:18.1	4.7(0.3) 7.4(0.5) 4.17(0.6) 4.30(1.1) 11.3(0.4)	–55.7(0.1) –53.1(0.1) –51.4(0.2) –50.6(0.1) –48.5(0.1)	2.2(0.3) 1.8(0.3) 0.9(0.6) 0.5(0.1) 3.1(0.2)	3.4	11.7
333.61–0.22 ^c	16:18:25.01	–49:59:08.1	3.0(0.4)	–49.7(0.2)	2.9(0.4)	3.4	11.8
335.59–0.29 ^a	16:27:15.40	–48:37:20.1	6.8(2.3) 10.2(2.4) 6.8(2.6) 22.3(2.2)	–47.5(0.1) –46.6(0.2) –46.3(0.1) –45.5(0.03)	0.9(0.3) 4.7(0.6) 0.5(0.2) 0.6(0.1)	3.3	12.2
336.41–0.26	16:30:31.51	–48:00:08.1	6.6(0.7) 24.8(0.9)	–89.7(0.1) –87.6(0.01)	1.4(0.2) 0.7(0.03)	5.3	10.3
337.40–0.41 ^a	16:35:08.01	–47:22:23.1	9.4(2.1) 16.5(2.4) 5.7(0.5)	–44.2(0.1) –42.3(0.1) –40.7(0.3)	0.4(0.1) 0.2(0.1) 7.4(0.8)	3.3	12.4
338.92+0.56 ^a	16:36:54.01	–45:36:05.0	18.4(1.8) 8.3(1.4)	–62.9(0.1) –60.1(0.2)	1.1(0.1) 1.5(0.4)	4.4	11.5
337.91–0.47 ^a	16:37:27.01	–47:02:10.1	58.2(2.4)	–43.6(0.01)	0.4(0.02)	3.3	12.4
341.19–0.22	16:48:39.50	–44:23:33.5	6.1(0.9)	–42.0(0.1)	0.7(0.1)	3.5	12.6
341.22–0.21 ^a	16:48:42.10	–44:21:53.0	15.6(1.0) 6.4(2.2)	–43.8(0.1) –43.0(0.1)	1.8(0.1) 0.4(0.2)	3.5	12.5
345.01+1.79 ^{a,b}	16:53:21.00	–40:09:40.0	25.6(1.1) 42.0(1.9)	–13.6(0.04) –13.1(0.01)	2.8(0.1) 0.5(0.03)	1.6	14.8
343.12–0.06 ^a	16:54:43.00	–42:47:49.0	46.6(3.0) 24.3(2.9) 22.1(1.9) 19.7(1.5)	–32.8(0.02) –31.5(0.02) –31.2(0.2) –27.3(0.02)	0.8(0.1) 0.5(0.1) 2.4(0.2) 0.7(0.1)	3.1	13.2
344.23–0.57 ^a	17:00:35.16	–42:14:29.7	12.0(0.8) 33.2(1.9)	–21.7(0.1) –20.3(0.02)	3.9(0.3) 0.6(0.1)	2.2	14.1
345.51+0.35	17:00:54.00	–40:40:02.0	4.6(0.3) 3.2(0.5) 2.3(0.6)	–17.1(0.1) –16.5(0.1) –14.7(0.1)	4.1(0.2) 0.9(0.2) 0.5(0.1)	2.0	14.4
345.00–0.22	17:01:38.51	–41:24:59.0	10.0(1.2) 10.0(1.2) 23.5(1.4) 3.4(1.1) 10.6(0.8)	–28.9(0.03) –28.0(0.1) –28.0(0.02) –26.0(0.6) –23.9(0.03)	0.6(0.1) 3.2(0.4) 0.7(0.1) 10.2(1.7) 1.2(0.1)	3.0	13.5
349.10+0.11	17:13:01.00	–37:56:06.0	6.4(1.6) 4.4(0.9)	–78.0(0.1) –77.3(0.2)	0.5(0.2) 2.3(0.4)	6.0	10.7
351.16+0.70 ^a	17:16:35.51	–35:54:44.0	22.2(5.9) 8.0(3.7) 11.8(8.6) 26.3(3.3)	–7.2(0.5) –7.1(0.1) –5.8(0.3) –4.9(0.03)	2.4(0.6) 0.3(0.2) 1.1(0.5) 0.6(0.1)	1.4	15.4
351.24+0.67	17:16:54.51	–35:51:58.0	4.3(0.4)	–4.5(0.1)	3.4(0.3)	0.1	16.1
351.41+0.64 ^a	17:17:32.35	–35:44:04.2	20.2(1.0) 7.0(1.3) 6.6(1.6)	–8.2(0.2) –6.4(0.1) –4.6(0.5)	4.2(0.3) 0.7(0.2) 3.6(0.8)	1.7 ³	

Table 1 – continued

Source	R.A. 1950 (h m s)	Dec. 1950 (° ′ ″)	Peak Flux Density (Jy)	LSR radial velocity (km s ⁻¹)	Line FWHM (km s ⁻¹)	Distance Near (kpc)	Distance Far (kpc)
NGC6334I(N) ^a	17:17:33.00	−35:42:04.0	42.6(4.0) 75.9(7.0) 77.9(5.7) 50.2(6.4) 52.7(4.1)	−7.5(0.03) −4.8(0.04) −4.8(0.01) −4.2(0.2) −3.0(0.03)	0.9(0.1) 1.7(0.2) 0.3(0.03) 5.4(0.3) 0.8(0.1)	1.7 ³	
351.78−0.54 ^a	17:23:20.67	−36:06:45.4	23.0(1.9) 36.0(2.2) 73.0(2.3) 26.8(1.2) 51.6(2.3) 22.2(1.6)	−8.3(0.02) −7.5(0.03) −6.9(0.01) −3.9(0.1) −2.4(0.01) −2.0(0.1)	0.5(0.1) 0.5(0.1) 0.4(0.03) 7.1(0.2) 0.4(0.02) 2.4(0.2)	1.5	15.3
351.64−1.26	17:25:55.00	−36:37:48.0	10.2(1.2)	−13.0(0.1)	1.2(0.2)	2.5	14.3
354.61+0.47 ^a	17:27:00.00	−33:11:38.0	9.6(2.1) 7.8(0.8) 24.0(1.7)	−21.4(0.04) −20.5(0.2) −17.9(0.02)	0.4(0.1) 3.0(0.3) 0.5(0.04)	4.0	12.9
353.41−0.36	17:27:07.00	−34:39:41.0	6.5(0.4) 8.1(0.8)	−17.4(0.1) −16.6(0.03)	5.0(0.3) 0.6(0.1)	3.4	13.5
SgrA−F ^a	17:42:27.40	−29:02:18.0	8.9(0.4) 4.1(1.2)	17.8(0.7) 23.9(0.3)	2.1(1.1) 4.2(1.1)		
359.62−0.25	17:42:30.00	−29:22:31.0	5.3(0.7) 15.9(1.1) 9.0(0.8)	17.7(0.1) 19.3(0.03) 20.6(0.1)	1.7(0.3) 0.6(0.1) 1.2(0.1)		
Sgr A−A ^a	17:42:41.30	−28:58:18.0	12.1(0.2)	42.1(0.2)	18.3(0.4)		
Sgr B2 ^a	17:44:10.60	−28:22:05.0	34.1(4.3) 7.8(0.3)	59.0(1.9) 70.5(3.4)	14.4(4.2) 8.2(9.0)	8.5 ⁴	
0.54−0.85	17:47:04.10	−28:54:01.0	4.1(0.9) 4.0(0.9) 4.7(0.3)	15.2(0.2) 16.9(0.1) 18.3(0.4)	2.3(0.4) 0.6(0.2) 4.1(0.7)	7.5	9.5
5.89−0.39 ^a	17:57:26.80	−24:03:54.0	9.5(0.8) 6.1(0.5) 9.2(1.3) 9.7(2.5)	8.5(0.1) 9.6(0.2) 11.6(0.03) 12.3(0.03)	1.2(0.1) 7.7(0.5) 0.4(0.1) 0.3(0.1)	2.4	14.5
M8E ^{a,b}	18:01:49.71	−24:26:56.0	129.7(2.0)	11.0(0.01)	0.5(0.01)	1.78 ⁵	
8.67−0.36	18:03:19.00	−21:37:59.0	4.9(0.7) 5.9(1.2) 4.3(1.0)	33.5(0.3) 35.0(0.2) 36.2(0.1)	1.5(0.5) 1.2(0.4) 0.6(0.2)	4.5	12.3
IRAS18056−1952	18:05:38.00	−19:52:34.0	9.5(0.9)	61.7(0.02)	0.4(0.1)	5.8	10.9
10.6−0.4	18:07:30.50	−19:56:28.0	8.1(0.9) 7.3(2.2) 3.9(0.6) 4.1(0.5) 3.2(0.3)	−7.6(0.3) −6.4(0.1) −4.7(0.1) −2.8(0.1) −1.4(0.7)	2.2(0.4) 1.2(0.2) 1.0(0.2) 1.7(0.3) 9.6(0.9)	2.0	18.7
12.89+0.49 ^b	18:08:56.40	−17:32:14.0	6.0(1.2) 5.7(1.1) 5.1(0.4)	29.6(0.04) 31.5(0.1) 32.9(0.2)	0.4(0.1) 0.4(0.2) 3.3(0.4)	3.5	13.1
11.94−0.62	18:11:04.40	−18:54:20.0	3.1(0.5) 2.7(0.6) 5.5(0.4)	35.0(0.1) 36.8(0.1) 38.5(0.1)	1.4(0.2) 0.6(0.2) 1.3(0.1)	3.9	12.7
W33MetC ^a	18:11:15.70	−17:56:53.0	21.2(3.1)	32.7(0.04)	0.5(0.1)	3.4	13.2
IRAS18141−1615	18:14:09.00	−16:15:47.0	4.0(1.1) 3.7(0.7) 7.2(1.0)	21.9(0.1) 23.1(0.3) 25.0(0.2)	0.8(0.3)	2.1	14.4
IRAS18151−1208	18:15:09.00	−12:08:34.0	3.3(0.4) 3.9(0.7)	32.2(0.1) 33.9(0.1)	1.3(0.2) 0.6(0.1)	2.8	13.4
14.33−0.64 ^a	18:16:00.80	−16:49:06.0	38.9(1.8) 32.2(2.0) 11.8(2.3) 50.1(1.8) 52.8(2.9)	19.1(0.02) 20.4(0.03) 21.3(0.1) 22.5(0.02) 23.4(0.02)	0.9(0.1) 0.7(0.1) 0.7(0.2) 1.0(0.1) 0.5(0.04)	2.6	13.9

**Figure 1.** 95-GHz spectra. All spectra are Hanning smoothed.

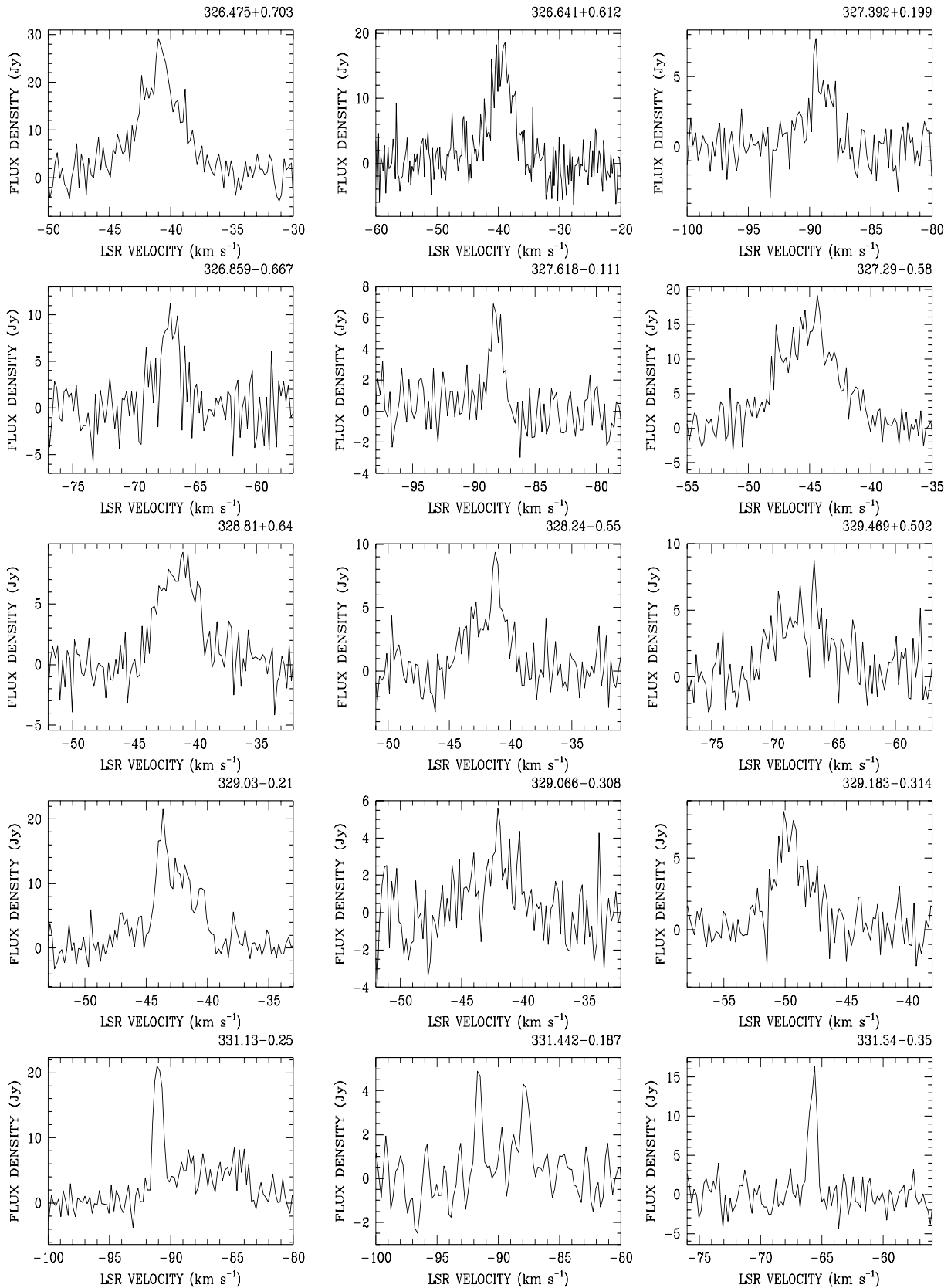
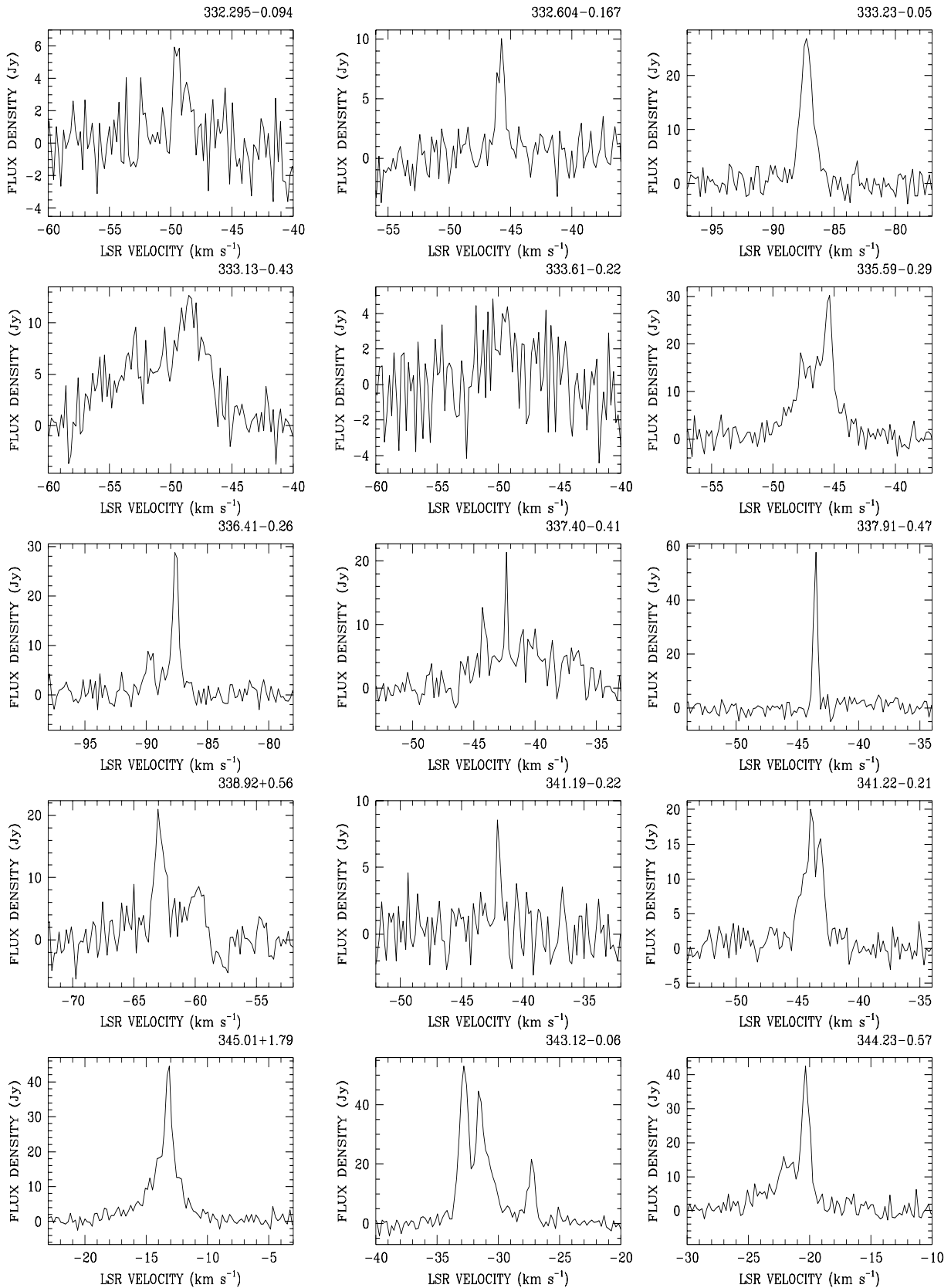


Figure 1 – *continued*

**Figure 1 – continued**

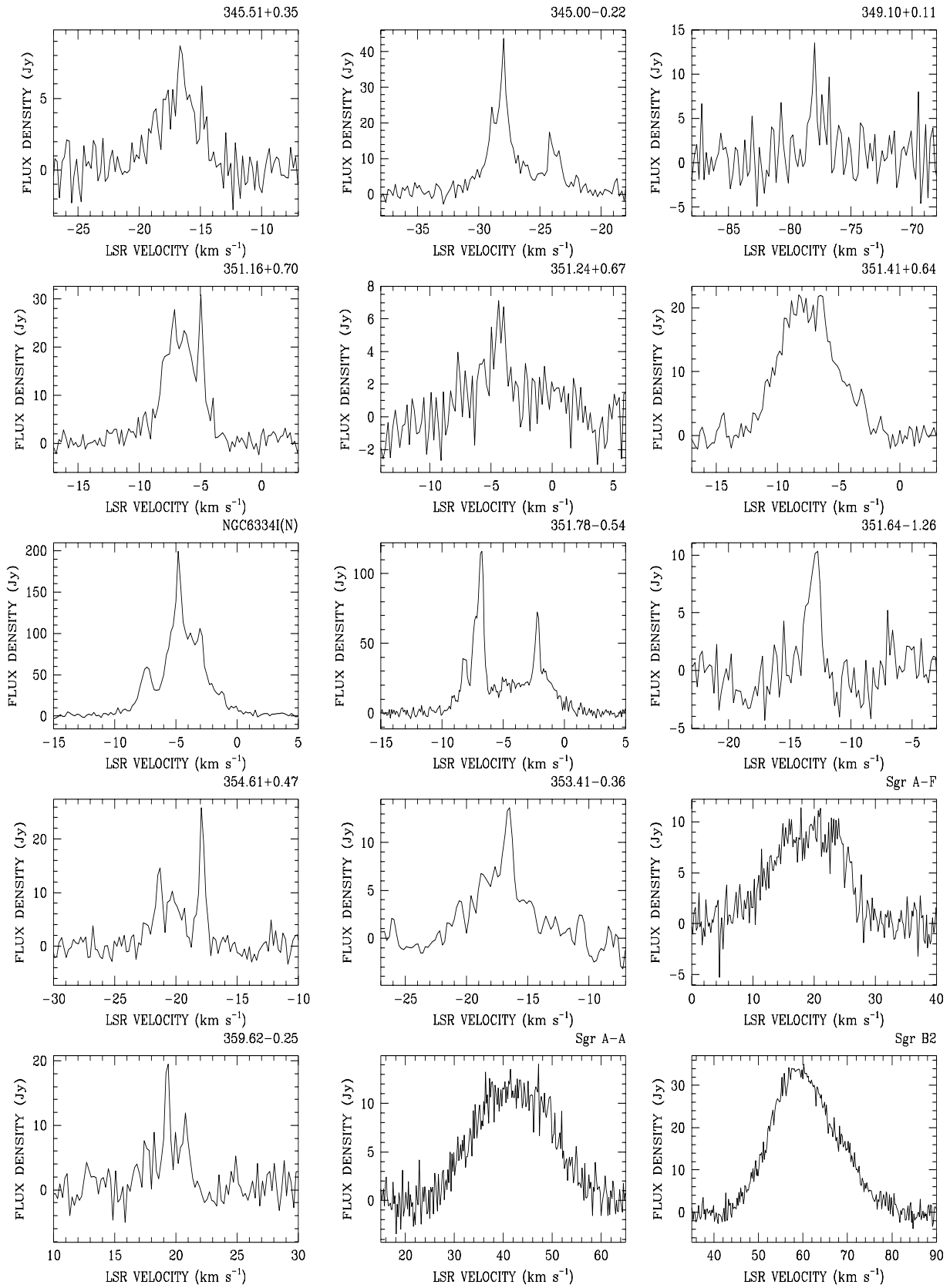
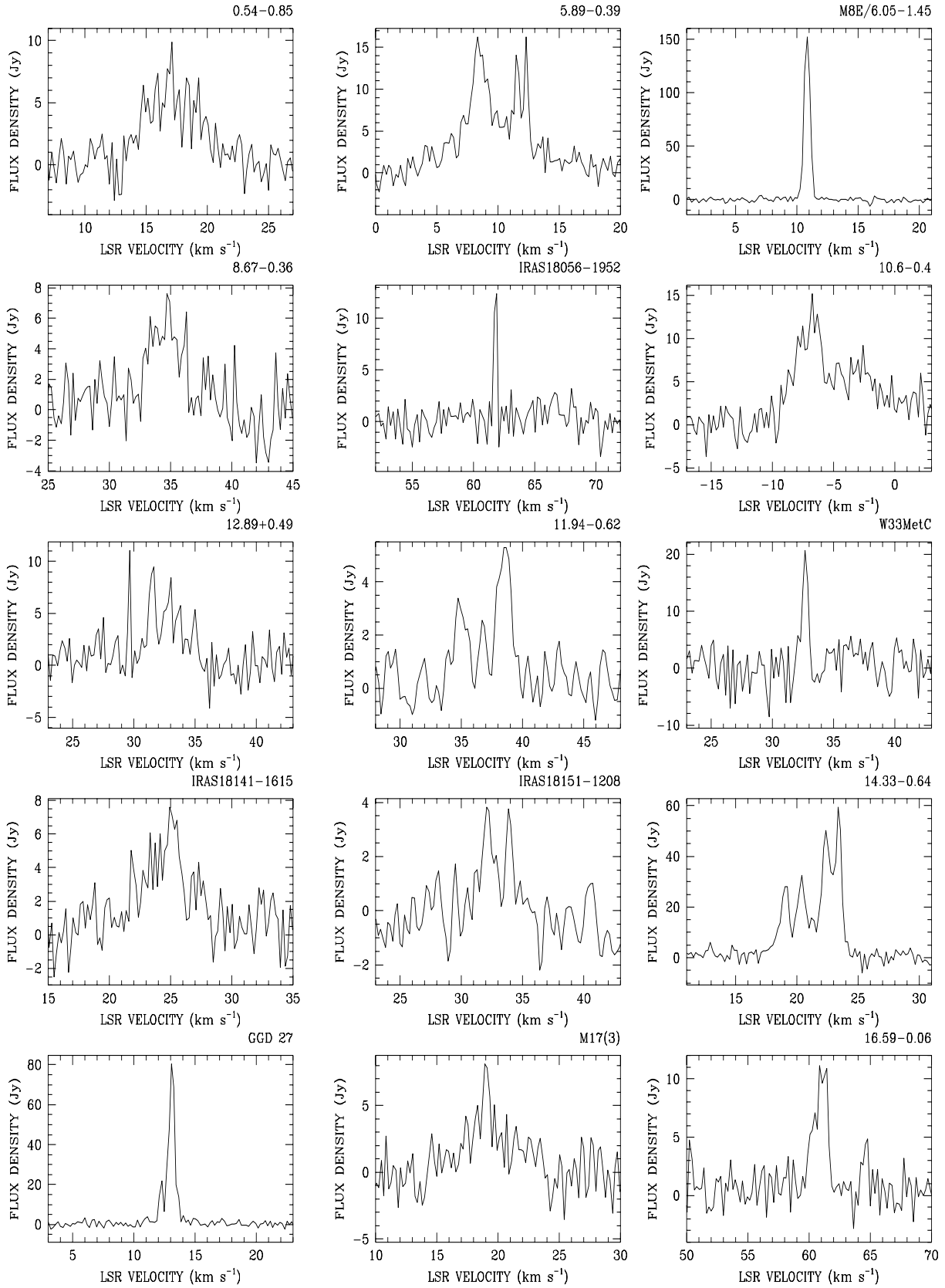


Figure 1 – continued

Figure 1 – *continued*

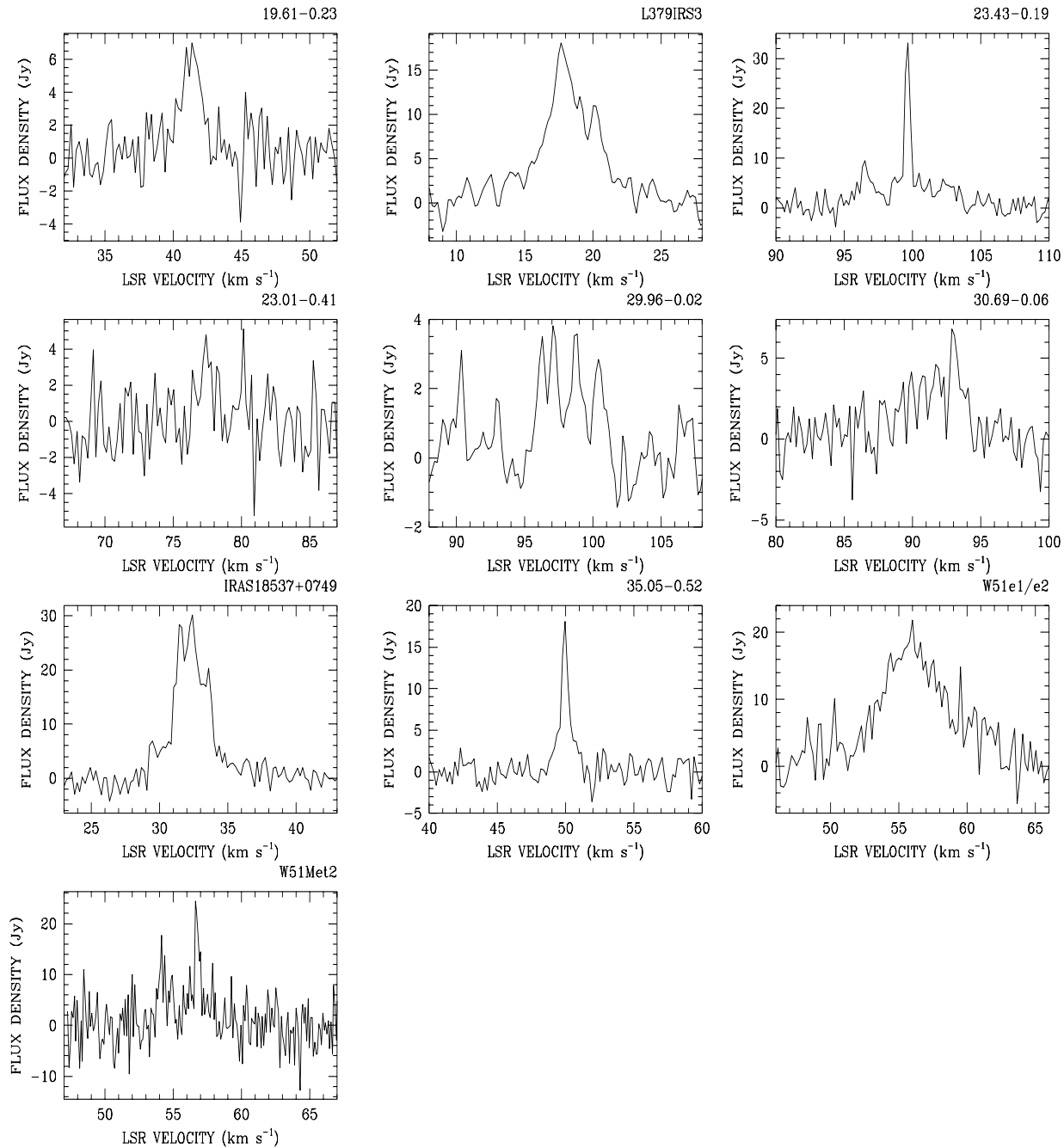
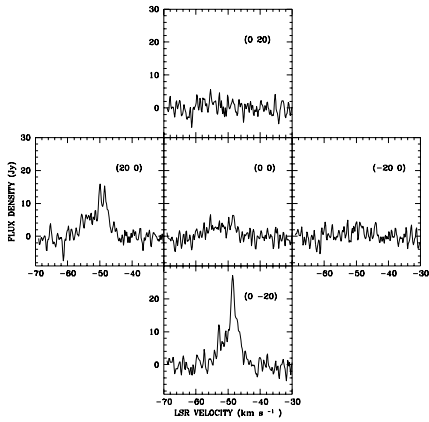
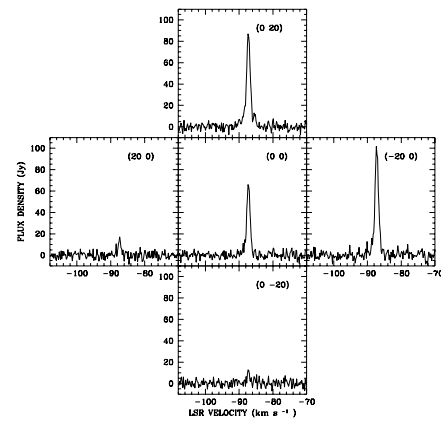


Figure 1 – *continued*

Table 1 – continued

Source	R.A. 1950 (h m s)	Dec. 1950 ($^{\circ}$ $'$ $''$)	Peak Flux Density (Jy)	LSR radial velocity (km s $^{-1}$)	Line FWHM (km s $^{-1}$)	Distance Near (kpc)	Distance Far (kpc)
GGD 27 ^{a,b}	18:16:13.80	-20:48:31.0	19.3(2.7) 33.4(3.9) 76.2(2.8) 14.8(3.2)	12.4(0.02) 12.9(0.02) 13.3(0.01) 13.7(0.02)	0.3(0.1) 0.3(0.04) 0.4(0.03) 0.2(0.1)	2.1	14.6
M17(3)	18:17:31.00	-16:12:50.0	1.9(1.9) 2.8(3.0) 2.8(0.5)	19.0(1.2) 19.1(0.1) 19.4(0.3)	2.0(1.6) 0.4(0.2) 5.4(0.7)	2.2	14.2
16.59-0.06	18:18:20.30	-14:33:18.0	5.7(1.1) 9.8(1.6)	60.4(0.2) 61.3(0.1)	1.1(0.4) 0.8(0.2)	4.7	11.6
19.61-0.23 ^a	18:24:50.30	-11:58:34.0	6.2(0.7)	41.3(0.1)	1.9(0.3)	3.4	12.6
L379IRS3	18:26:32.90	-15:17:58.0	3.9(0.8) 4.6(1.3) 10.1(1.2) 6.0(0.8)	17.8(0.3) 17.7(0.1) 18.0(0.1) 20.3(0.1)	9.2(1.2) 0.7(0.2) 2.7(0.3) 0.9(0.2)	1.7	14.6
23.43-0.19 ^a	18:31:55.80	-08:34:17.0	7.0(1.4) 33.8(2.5)	96.6(0.2) 99.6(0.02)	1.7(0.4) 0.5(0.04)	5.8	9.8
23.01-0.41 ^c	18:31:56.70	-09:03:18.0	3.4(0.6)	77.4(0.1)	1.3(0.3)	4.9	10.8
29.96-0.02	18:43:27.10	-02:42:36.0	3.3(0.6) 3.8(0.6) 3.2(0.5) 2.8(0.7)	96.2(0.1) 97.1(0.1) 98.7(0.1) 100.4(0.1)	0.7(0.2) 0.7(0.2) 1.1(0.2) 0.9(0.2)	6.1	8.6
30.69-0.06	18:44:58.90	-02:04:27.0	3.2(0.3) 3.8(0.7)	91.4(0.2) 93.1(0.1)	5.0(0.4) 0.6(0.2)	5.3	9.3
IRAS18537+0749 ^a	18:53:46.00	07:49:16.0	5.9(1.1) 26.7(2.2) 22.3(5.0) 18.4(1.3)	30.0(0.3) 31.5(0.1) 32.3(0.1) 33.3(0.1)	1.6(0.6) 0.9(0.2) 0.6(0.2) 1.5(0.2)	2.2	10.8
35.05-0.52 ^a	18:54:37.10	01:35:01.0	16.1(1.1)	49.9(0.02)	0.7(0.1)	3.3	10.6
W51e1/e2	19:21:26.20	14:54:43.0	17.7(0.5) 4.8(0.7)	55.9(0.1) 61.1(0.2)	5.3(0.2) 2.6(0.5)	5.4	
W51Met2 ^{a,b}	19:21:28.90	14:23:48.0	10.5(2.0) 19.7(2.6)	54.2(0.1) 56.7(0.04)	1.0(0.2) 0.6(0.1)	5.5	

**Figure 2.** Map of 333.13-0.43.**Figure 3.** Map of 333.23-0.05.

right ascension. The 95-GHz maser spectrum is similar to that at 44 GHz, where it is a factor of 3 stronger.

335.59-0.29. The 95-GHz spectrum of this source is best fitted with 4 Gaussian components, while at 44 GHz only one intense component is present at the same radial velocity as the strongest 95-GHz component.

337.91-0.47. The 95-GHz methanol maser spectrum is

essentially identical to the 44-GHz spectrum, but the peak flux density at 44 GHz is a factor of four higher.

338.92+0.56. The 95-GHz spectrum of this source has two narrow features, at radial velocities -62.9 km s $^{-1}$ and -60.1 km s $^{-1}$, the same as the 44-GHz spectrum (Slysh et al. 1994). However, a five-point map centred on the nominal position of the source (Fig. 4) shows that the strongest emission is to the north, where the flux density is at least

Table 2. Sources undetected at 95 GHz.

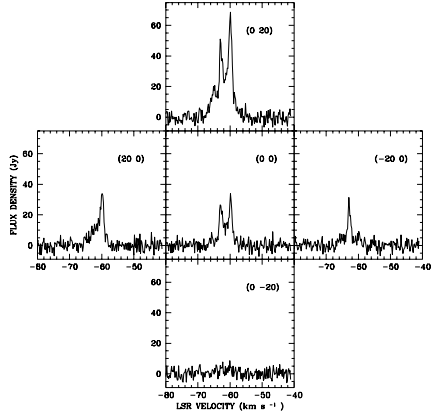
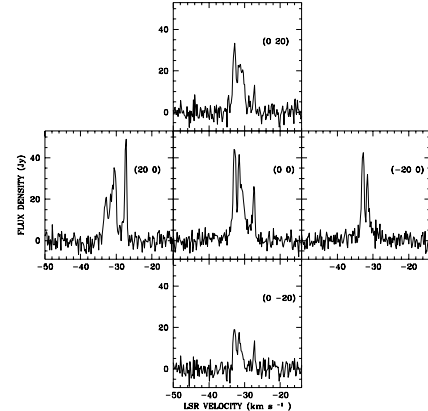
Source	R.A. 1950 (h m s)	Dec. 1950 ($^{\circ}$ $'$ $''$)	LSR radial velocity (km s $^{-1}$)	3- σ (Jy)	Distance	
					Near (kpc)	Far (kpc)
175.84–21.48	04:16:08.98	19:17:54.9	0.00	7.4	0.1	17.1
176.23–20.87	04:19:06.98	19:25:44.9	0.00	8.0	0.1	17.1
N105	05:10:12.64	–68:57:07.8	250.70	1.6		
210.42–19.76	05:33:53.17	–06:46:49.9	10.00	9.0	1.2	15.8
205.45–14.55	05:43:35.87	–00:09:25.9	10.00	7.1	1.3	16.7
213.83+0.62	06:52:43.57	–00:27:11.0	10.00	8.3	1.1	15.2
232.62+1.00	07:29:54.97	–16:51:47.0	23.00	10.6	1.1	15.2
233.76–0.19	07:27:52.67	–18:26:08.0	43.00	5.9	4.2	14.3
243.16+0.37	07:50:18.37	–26:17:53.0	52.00	6.5	5.3	13.0
254.66+0.21	08:18:54.06	–36:03:00.0	64.00	5.8	7.2	11.7
IRAS08337–4028	08:33:42.40	–40:28:01.8	–2.00	5.2	0.3	3.2
263.25+0.52	08:47:00.46	–42:43:15.0	13.00	6.5	2.7	4.7
IRAS08546–4254	08:54:36.20	–42:54:06.0	9.00	2.8	2.3	4.0
IRAS09015–4843	09:01:33.20	–48:43:25.4	56.00	4.4	8.0	
IRAS09018–4816	09:01:50.30	–48:15:57.9	16.00	2.7	3.7	4.0
IRAS09149–4743	09:14:54.10	–47:43:13.0	4.00	3.6	2.2	
284.35–0.42	10:22:20.00	–57:37:25.0	7.00	3.0	1.4	5.6
285.32–0.03	10:30:04.23	–57:47:50.1	0.60	2.9	0.5	5.0
IRAS10303–5746	10:30:21.36	–57:46:44.0	1.00	3.7	0.6	5.1
IRAS10460–5811	10:46:06.30	–58:11:12.4	–2.00	3.0	0.1	5.2
IRAS10555–6242	10:55:34.80	–62:42:49.8	–16.00	2.6	2.4	3.5
IRAS11097–6102	11:09:46.70	–61:02:06.0	–30.00	3.1	2.9	
291.58–0.43	11:12:58.10	–60:53:40.0	11.00	3.8	1.5	7.8
293.84–0.78	11:29:49.60	–61:58:12.5	36.90	3.5	3.9	10.7
293.95–0.91	11:30:22.70	–62:07:22.2	41.40	3.9	4.3	11.2
IRAS11332–6258	11:33:15.00	–62:58:13.0	–10.00	3.4	0.8	6.3
298.22–0.33	12:07:16.90	–62:33:01.0	31.80	3.8	3.2	11.2
299.01+0.13	12:14:42.90	–62:12:21.0	19.00	3.8	2.0	10.2
IRAS12272–6240	12:27:15.90	–62:40:25.0	8.00	5.6	1.0	9.6
IRAS13080–6229	13:08:05.54	–62:29:58.1	–33.00	3.7	2.9	6.9
IRAS13111–6228	13:11:07.49	–62:28:31.7	–37.00	4.8	3.3	6.5
308.92+0.12	13:39:35.40	–61:53:47.0	–30.00	2.7	2.3	8.4
IRAS13504–6151	13:50:27.70	–61:51:37.3	3.00	2.9	0.4	11.4
311.96+0.14	14:04:19.70	–61:08:34.0	–30.00	3.8	2.1	9.6
IRAS14050–6056	14:05:05.40	–60:56:29.0	–50.00	2.8	4.0	7.4
IRAS14159–6038	14:16:00.50	–60:38:00.0	–10.00	2.5	0.6	11.1
318.05+0.09	14:49:52.91	–58:56:47.1	–49.51	3.2	3.4	9.2
318.94–0.20	14:57:01.50	–58:47:14.2	–36.10	4.1	2.5	10.4
322.17+0.62	15:14:50.20	–56:27:51.1	–53.86	3.4	3.6	9.8
326.66+0.57	15:40:59.00	–53:57:24.1	–41.23	3.4	2.8	11.4
326.662+0.521	15:41:12.87	–53:59:39.4	–41.00	4.8	2.8	11.4
327.590–0.094	15:48:45.38	–53:54:22.8	–86.30	2.4	5.4	8.9
327.945–0.115	15:50:42.65	–53:41:55.7	–51.70	2.8	3.4	11.0
328.20–0.58	15:54:02.31	–53:53:37.1	–40.79	3.5	2.8	11.7
329.339+0.148	15:56:43.74	–52:36:13.6	–106.50	2.5	7.3	
329.622+0.138	15:58:11.08	–52:25:38.2	–60.10	3.2	3.9	10.8
329.610+0.114	15:58:13.81	–52:27:12.8	–60.10	3.2	3.9	10.8
331.425+0.264	16:06:22.14	–51:08:14.9	–88.60	3.2	5.4	9.6
331.120–0.118	16:06:34.50	–51:37:31.3	–65.00	3.0	4.2	10.7
332.094–0.421	16:12:28.14	–51:10:59.6	–61.40	3.1	4.0	11.0
332.351–0.436	16:13:43.46	–51:01:00.6	–53.10	2.6	3.6	11.5
332.560–0.148	16:13:25.00	–50:39:50.1	–51.00	2.7	3.5	11.6
335.78+0.17	16:26:03.00	–48:09:44.1	–48.53	3.5	3.5	12.0
339.88–1.26	16:48:24.76	–46:03:34.0	–31.87	3.5	2.8	13.2
345.41–0.94	17:06:02.01	–41:31:44.0	–22.86	2.6	2.6	13.9
348.18–0.49	17:08:39.01	–38:27:06.0	–7.18	3.1	1.1	15.9
IRAS17424–2859	17:42:29.00	–28:59:20.0	28.80	3.3		
IRAS17432–2855	17:43:16.00	–28:55:05.0	51.90	2.2		
IRAS17433–2841	17:43:21.00	–28:41:15.0	34.80	2.9		

Table 2 – continued

Source	R.A. 1950 (h m s)	Dec. 1950 ($^{\circ}$ $'$ $''$)	LSR radial velocity (km s $^{-1}$)	3- σ (Jy)	Distance	
					Near (kpc)	Far (kpc)
IRAS17470–2853	17:47:04.00	–28:53:13.0	17.30	2.6	7.4	9.6
25.53+0.38	18:33:51.38	–06:26:59.4	95.60	2.7	5.7	9.7
25.41+0.09	18:34:37.30	–06:41:42.7	97.40	2.5	5.7	9.6
25.48+0.06	18:34:53.26	–06:38:34.8	95.50	2.8	5.7	9.7
25.82–0.18	18:36:21.78	–06:27:24.2	91.70	3.1	5.5	9.8
26.57–0.25	18:38:00.13	–05:49:14.4	103.80	3.3	6.1	9.1
29.98–0.04	18:43:35.00	–02:42:19.0	102.60	3.0	6.4	8.3
IRAS18449–0115	18:44:59.00	–01:15:59.0	97.80	6.4	6.3	8.3
IRAS18469–0132	18:46:59.00	–01:32:38.0	84.60	2.6	5.3	9.2

Table 3. Comparison between Mopra and Onsala observations of 95 GHz sources.

Source name	Mopra LSR radial velocity (km s $^{-1}$)	Mopra Line width (km s $^{-1}$)	Mopra Flux density (Jy)	Onsala LSR radial velocity (km s $^{-1}$)	Onsala Line width (km s $^{-1}$)	Onsala Flux density (Jy)
OMC-2	11.4	0.3	138(7.0)	11.4	1.1	69.9(1.1)
NGC2264	7.3	0.2	99.2(5.7)	7.7	1.0	46.2(1.7)
W33MetC	32.7	0.5	21.2(3.1)	32.3	1.6	12.6(1.8)
L379IRS3	18.0	2.7	10.1(1.2)	18.2	3.9	21.3(1.3)
W51e1/e2	55.9	5.3	17.7(0.5)	55.9	9.5	21.8(2.0)
W51Met2	56.7	0.6	19.7(2.6)	56.5	1.2	9.4(0.9)

**Figure 4.** Map of 338.92+0.56.**Figure 5.** Map of 343.12-0.06.

a factor of two higher. From the spectrum of the offset (0, 20'') one can see also a third detail, at the radial velocity -65.2 km s $^{-1}$, which is not present in the 44-GHz spectrum. The five-point map also shows that the position of the spectral feature at -60.1 km s $^{-1}$ is shifted in right ascension relative to the spectral feature at -62.9 km s $^{-1}$ by about 20''.

343.12-0.06. The 95-GHz spectrum of this source has been fitted with four Gaussian components, all of which have counterparts in the 44-GHz spectrum (Slysh et al. 1994), although the relative intensities are different at the two frequencies. A five-point map of the source (Fig. 5) shows that the emission in the source is spread over an area of at least 20'', so the difference in relative intensities is most likely due to the different telescope beamwidths and pointing errors between the 44- and 95-GHz observations.

345.01+1.79 The 95-GHz spectrum of this source has been fitted by two Gaussians separated by 1.2 km s $^{-1}$. A 9-point map of this source (Val'tts 1998) was used to determined position of both components. The stronger component at -13.1 km s $^{-1}$ has a position which coincides within the errors with the position of the southern 6.7-GHz methanol maser (Norris et al. 1993). The weaker component at -14.3 km s $^{-1}$ is displaced from the stronger one by $-6.6 \pm 7.9''$ in right ascension and $10.2 \pm 5.3''$ in declination, and coincides within the errors with the position of the northern 6.7-GHz methanol maser. Thus 95-GHz methanol masers are present in both regions of methanol maser emission in this source.

345.00-0.22. The 95-GHz methanol maser spectrum is similar to that at 44 GHz, except for the presence of an

Table 4. Comparison between Mopra and Parkes observations at 44 GHz sources.

Source name	LSR radial velocity (km s ⁻¹)	Mopra Line width (km s ⁻¹)	Flux density (Jy)	LSR radial velocity (km s ⁻¹)	Parkes Line width (km s ⁻¹)	Flux density (Jy)
269.20-1.13	9.4	0.7	15.1(2.3)	9.4	0.3	23.2(1.6)
270.26+0.84	9.3	0.6	7.0(3.1)	9.7	0.3	37.0(6.3)
294.97-1.73	-8.2	1.3	5.9(0.8)	-8.25	0.9	12.2(2.0)
305.21+0.21	-42.3	0.6	26.1(2.0)	-42.3	0.5	75.7(3.7)
305.36+0.20	-33.4	0.9	17.4(1.4)	-33.1	0.6	106(8.9)
316.76-0.02	-39.4	0.7	12.9(1.6)	-39.3	0.4	26.9(2.2)
320.28-0.31	-66.3	0.7	14.5(1.9)	-66.3	0.9	45.4(3.2)
323.74-0.27	-49.8	2.9	4.9(0.4)	-49.9	0.4	23.1(4.2)
324.72+0.34	-50.6	2.5	3.1(0.5)	-51.8	0.4	43.8(3.7)
327.29-0.58	-44.6	2.5	14.3(1.1)	-44.3	0.9	26.1(3.1)
328.81+0.64	-40.9	3.1	7.2(0.9)	-40.6	1.2	23.5(1.6)
328.24-0.55	-41.2	1.8	7.3(0.4)	-41.1	0.3	11.8(2.2)
329.03-0.21	-43.7	1.3	19.3(1.3)	-43.7	0.7	24.9(3.5)
331.13-0.25	-91.0	1.0	20.5(0.7)	-91.0	0.7	95.0(4.4)
331.34-0.35	-65.7	0.7	15.8(1.3)	-65.7	0.4	24.0(5.5)
333.23-0.05	-87.2	1.3	99.3(2.3)	-87.2	1.3	205(6.6)
333.13-0.43	-48.6	1.0	17.0(2.1)	-48.2	0.8	98.5(3.8)
333.61-0.22	-49.7	2.9	3.0(0.4)	-49.3	0.6	21.2(2.5)
335.59-0.29	-45.5	0.6	22.3(2.2)	-45.4	0.6	158(4.5)
336.41-0.26	-87.6	0.7	24.8(0.9)	-87.6	0.7	51.4(3.7)
337.40-0.41	-42.3	0.2	16.5(2.4)	-42.3	0.2	26.8(2.3)
338.92+0.56	-62.7	1.8	43.3(1.9)	-62.9	0.5	166(5.4)
337.91-0.47	-43.6	0.4	58.2(2.4)	-43.4	0.4	273(4.0)
341.19-0.22	-42.0	0.7	6.1(0.9)	-41.9	0.3	92.9(2.9)
341.22-0.21	-43.8	1.8	15.6(1.0)	-43.8	0.4	25.5(6.8)
345.01+1.79	-13.1	0.5	49.6(1.9)	-13.2	0.4	33.4(2.7)
343.12-0.06	-32.8	0.8	46.6(3.0)	-32.8	1.0	71.9(2.2)
344.23-0.57	-20.3	0.6	33.2(1.9)	-20.3	0.6	48.4(9.6)
345.51+0.35	-16.5	0.9	3.2(0.5)	-16.5	0.6	16.2(1.6)
345.00-0.22	-28.0	0.7	23.5(1.4)	-27.9	0.6	69.3(9.4)
349.10+0.11	-78.0	0.5	6.4(1.6)	-77.9	0.3	23.8(2.1)
351.16+0.70	-4.9	0.6	26.3(3.3)	-4.5	0.4	36.9(9.9)
351.24+0.67	-4.5	3.4	4.3(0.4)	-4.5	0.3	21.5(0.8)
351.41+0.64	-8.2	4.2	20.2(1.0)	-8.4	1.4	39.9(1.9)
351.78-0.54	-6.9	0.4	73.0(2.3)	-6.9	0.4	150(4.6)
351.64-1.26	-12.7	0.7	15.2(2.5)	-13.1	1.2	12.7(1.1)
354.61+0.47	-17.9	0.5	24.0(1.7)	-17.8	0.5	55.5(9.8)
353.41-0.36	-16.6	0.6	8.1(0.8)	-16.5	0.6	31.4(3.5)
359.62-0.25	19.3	0.6	15.9(1.1)	19.4	0.4	105(5.2)
0.54-0.85	16.9	0.6	4.0(0.9)	14.8	0.7	33.8(1.7)
M8E	11.0	0.5	129.7(2.0)	10.9	0.4	510(34.2)
12.89+0.49	31.5	0.4	5.7(1.1)	31.4	0.3	24.4(2.2)
14.33-0.64	23.4	0.5	52.8(2.9)	23.5	0.5	120(9.8)
16.59-0.06	61.3	0.8	9.8(1.6)	61.2	0.2	12.5(2.5)
23.43-0.19	99.6	0.5	33.6(2.1)	99.7	0.4	78.9(6.1)
23.01-0.41	77.4	1.3	3.4(0.6)	77.1	0.3	32.2(2.8)
30.69-0.06	89.3	0.6	3.8(0.6)	89.5	0.5	29.8(7.7)

additional feature at -24 km s⁻¹, which is absent from the 44-GHz spectrum.

351.16+0.70 (NGC6334B). The 95-GHz spectrum is similar to 44-GHz spectrum, although due to blending of spectral features the number of Gaussian components we are able to fit is different, 4 at 95 GHz compared to 7 at 44 GHz.

351.24+0.67 (NGC6334C). The 95-GHz emission from this source is anomalously low compared to 44-GHz emission (Slysh et al. 1994), possibly due to poor pointing, or variable weather conditions.

351.41+0.64 (NGC6334F). A broad line with some weaker narrow features is present in the 95-GHz spectrum; we have fitted the profile with two broad components and one narrow at the radial velocity -6.4 km s⁻¹. It is probably the counterpart of the -6.32 km s⁻¹ component in the 44-GHz spectrum (Slysh et al. 1994), but other narrow 44-GHz features are not present in the 95-GHz spectrum.

NGC6334I(N). This is one of the strongest methanol masers at both 95- and 44-GHz (Haschick et al. 1990). The spectra are similar at the two frequencies, considering likely

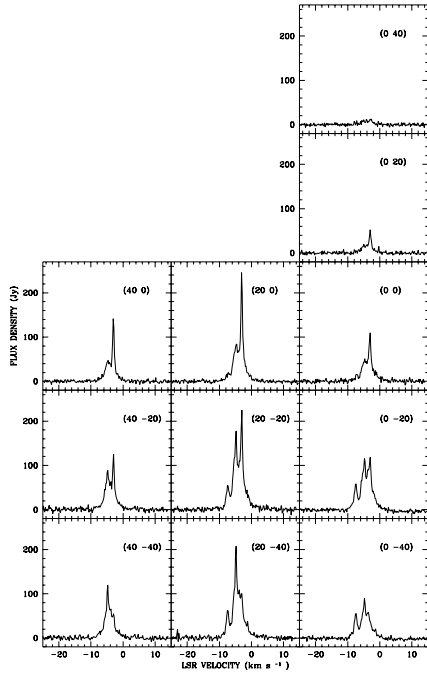


Figure 6. Map of NGC6334I(N).

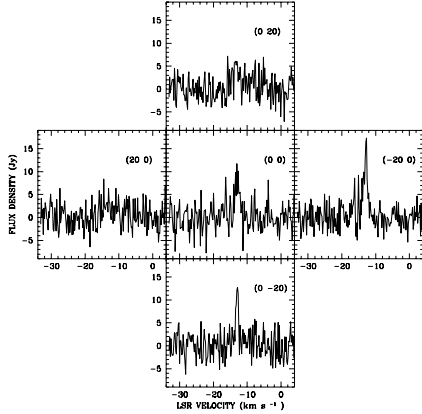


Figure 7. Map of 351.64-1.26.

differences in pointing, since the maser is known to be spread over an area more than $30''$ in extent as can be seen from our map (Fig. 6). The relative positions of the four strongest spectral features were determined from this map and are given in Table 5. A comparison with the map of the source at 44 GHz (Kogan & Slysh 1998) shows that there is a general agreement between the two maps if larger position errors of 95-GHz map are taken into account. All four spectral features are point-like within the Mopra beamwidth of $52''$.

351.64-1.26. A five-point map of this source shows that the single weak feature becomes stronger at offsets of $(-20'', 0)$ and $(0, -20'')$ (Fig. 7), which implies that the true source position is to the south-east of the the nominal position.

351.78-0.54. The 95-GHz spectrum consists of four narrow components, all of which are present in the 44-GHz spectrum, and in addition there is a broad component about 8 km s^{-1} wide, which is absent at 44 GHz.

354.61+0.47. At least three Gaussian components can

Table 5. Position of components in NGC6334I(N)

N	LSR radial velocity (km s ⁻¹)	Line width (km s ⁻¹)	$\Delta\alpha$ (")	$\Delta\delta$ (")	Flux density (Jy)
1	-7.5	0.8	9(5)	-30(5)	44
2	-4.8	0.8	18(1)	-35(5)	110
3	-4.0	4.0	18(5)	-28(5)	100
4	-3.0	0.5	24(6)	-12(7)	175

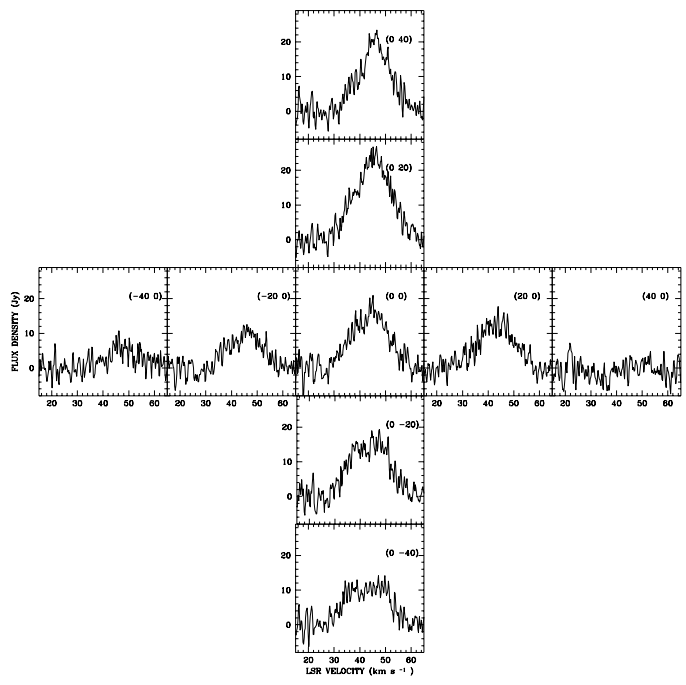


Figure 8. Map of Sgr A-A.

be fitted to the 95-GHz spectrum of this source, and two of them are present in the 44-GHz spectrum. The component at -21.4 km s^{-1} is relatively stronger at 95 GHz and the component at -20.5 km s^{-1} is present only at 95 GHz.

Sgr A-A. The 95-GHz spectrum of this source consists of a very broad component and possibly a weak narrow component at a velocity of 47 km s^{-1} . It is almost identical to the 44-GHz spectrum (Haschick et al. 1990), with the narrow component relatively stronger at 44 GHz. A 9-point map (Fig. 8) of the source does not show the narrow component, probably because of the shorter integration time of map spectra. The broad component is extended in declination with an angular size of $150''$, and is unresolved (less than $30''$) in right ascension. This is one of the rare strong thermal sources in our sample.

M8E. A single very strong narrow line is present in the 95-GHz spectrum, which is similar to that at 44 GHz. This is one of the strongest masers in both the 44- and 95-GHz transitions, and its angular extent is known to be less than $0.2''$ (Kogan & Slysh 1998, Slysh et al. 1999). A thorough discussion of the methanol emission from this source is given in Val'tts (1999a).

W33MetC. A single feature near 32.5 km s^{-1} is present in 95-GHz spectrum. At 44 GHz there is also a weaker com-

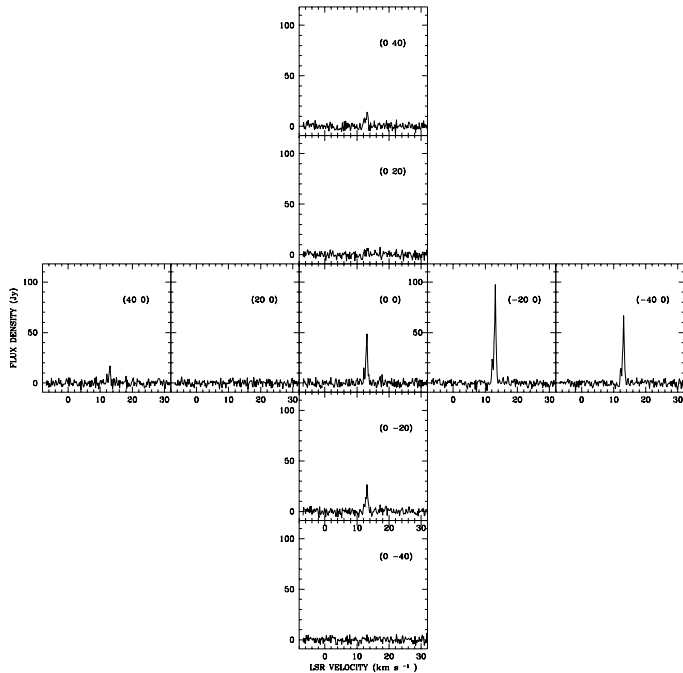


Figure 9. Map of GGD27.

ponent at 36.28 km s^{-1} which is not visible in 95-GHz spectrum. The 95-GHz emission in this source has been mapped by Pratap & Menten (1992), and the corresponding 44-GHz maser has been shown to coincide with its position (Slysh et al. 1999). A full discussion of the methanol emission from this source is given by Val'tts (1999b).

14.33-0.64. This intense class I methanol maser was discovered at 44 GHz at Parkes (Slysh et al. 1994). At 95-GHz the maser is also strong and its spectrum consists of four peaks, similar to the 44-GHz spectrum. A 44-GHz map of this maser is discussed in Slysh et al. (1999).

GGD27. 44-GHz class I methanol maser emission in this source was discovered by Kalenskii et al. (1992), and a VLA map of it is presented in Slysh et al. (1999). At both 95 and 44 GHz the spectrum is dominated by a strong narrow feature. A 9-point map of the 95-GHz emission (Fig. 9) shows that it is strongest at a position offset in right ascension by $-23'' \pm 8''$ and in declination by $-8'' \pm 5''$ from the nominal position.

L379IRS3. The 44-GHz methanol maser associated with this source was also discovered by Kalenskii et al. (1992) and mapped with the VLA by Kogan & Slysh (1998) and Slysh et al. (1999). The 95-GHz spectrum is very similar to that at 44 GHz and a map (Fig. 10) of the 95-GHz emission shows that the four spectral features are spread over an area of approximately $30''$, similar to the 44-GHz emission.

23.43-0.19. Two Gaussian components have been fitted to the detection at 95 GHz of this source, both are present in the 44-GHz spectrum (Slysh et al. 1994). In addition there are several components near 103 km s^{-1} in the 44-GHz spectrum that are not present at 95 GHz.

IRAS18537+0749 (S76E). This rather strong source was discovered to be a class I methanol maser during observations of the $4_{-1} - 3_0 E$ transition at 36 GHz at Puschino (Val'tts, private communication). In both transitions it ap-

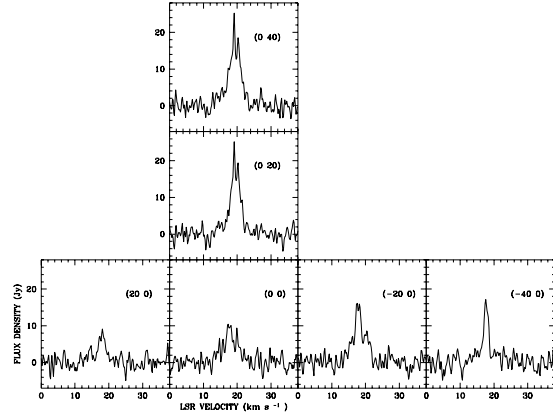


Figure 10. Map of L379IRS3.

pears that a blend of several narrow lines is producing a spectrum resembling a wide band of emission.

W51e1/e2. Only a broad component is present in our 95-GHz spectrum. The narrow spectral feature at 48.88 km s^{-1} detected by Haschick et al. (1990) at 44 GHz is not visible in the 95-GHz spectrum, because it is shifted from W51e1/e2 by about $70''$ and was outside the main beam of Mopra telescope (Pratap & Menten 1992).

4 DISCUSSION

The spectra of the 95-GHz $8_0 - 7_1 A^+$ methanol emission sources found in this survey are in general similar to the spectra of the corresponding 44-GHz $7_0 - 6_1 A^+$ sources. The emission in the two transitions typically covers the same velocity range, has approximately the same number of spectral features with very similar radial velocities, and in some cases even the same relative intensities of the components. In Table 4 we list the single strongest feature in each spectrum at 95 GHz and the corresponding spectral features at 44 GHz of the sources detected by Slysh et al. (1994). One can see that there is always a corresponding spectral feature at 44 GHz to every 95 GHz spectral feature from Table 5, and their radial velocities agree in general to within 0.1 km s^{-1} . The line width of the 95-GHz components is in general somewhat larger than the line width of the corresponding 44-GHz features, partly due to a lower spectral resolution in the 95 GHz observations, but nevertheless there are many very narrow 95-GHz features with a line width less than 1 km s^{-1} . The peak flux density of the 95-GHz components is generally lower than the flux density of the 44-GHz features. Fig. 11 shows a comparison between the flux densities of spectral features with the same radial velocities from the two transitions. In constructing this plot data on all available sources were used, including the results of this work and of the observations at Onsala (Val'tts et al. 1995). The straight line (with a correlation coefficient $r=0.73$) shows the best fit linear dependence which was found to be :

$$S(95) = (0.32 \pm 0.08) \times S(44) - (8.1 \pm 2.7) \quad (1)$$

Although the scatter is quite large, on average the 95-GHz methanol masers are a factor of 3 weaker than the 44-GHz masers. This result is consistent with the findings of Val'tts et al. (1995) who found a linear dependence between integrated fluxes at two frequencies. We have used

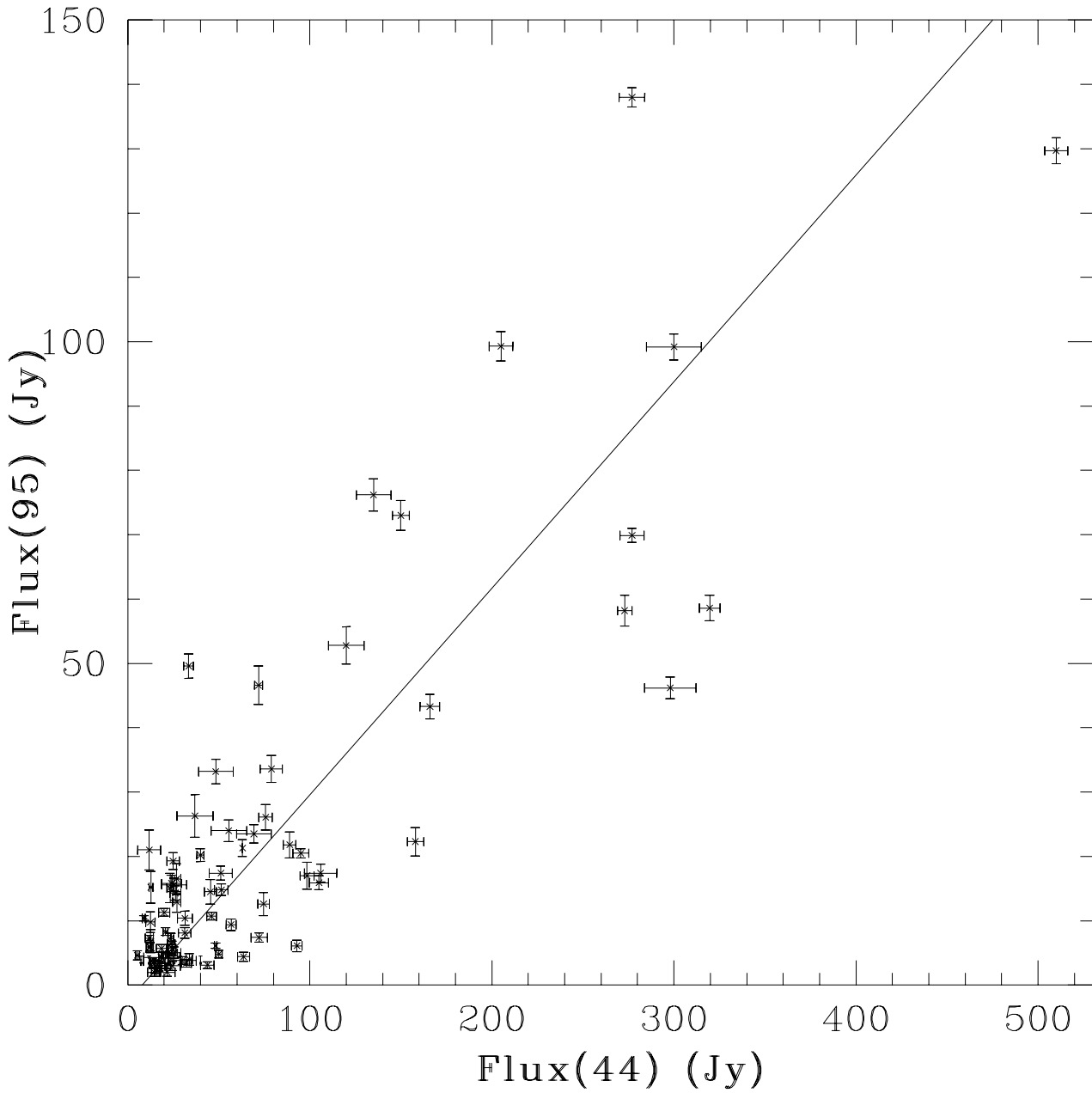


Figure 11. A correlation between 95 GHz and 44 GHz peak flux density. Straight line is a best fit: $y = (0.32 \pm 0.08)x - (8.1 \pm 2.7)$, correlation coefficient - $r = 0.73$.

peak flux densities rather than luminosities since our survey is flux density limited by the sensitivity of the instrument, and luminosities would give a spurious correlation due to the multiplication of the flux densities at the two frequencies by the same distance squared. The slope of the dependence between integrated flux densities found by Val'tts et al. (1995) is 0.52 ± 0.05 , which is larger than the slope 0.32 ± 0.08 found in this paper for the peak flux densities. This difference may be due to the larger average line width of 95-GHz masers mentioned above. The correlation between the peak flux density and the observed similarity in the spectra of the two transitions is strong evidence in favour of the suggestion

that the emission from both transitions arises from the same spatial location. A comparison of published high resolution maps of the 44- and 95-GHz class I methanol masers in DR21(OH) and W33MetC shows that their images are very alike and consist of the same number of isolated maser spots (Plambeck & Menten 1990, Pratap & Menten 1992, Kogan & Slysh 1998, Slysh et al. 1999), consistent with this hypothesis.

The two transitions belong to the class I methanol masers (Menten 1991), which are thought to be pumped through collisional excitation. The difference between the two transitions is that the upper level of the 95-GHz $8_0 -$

Table 6. LVG calculation results: ratios of 44/95 intensities for four models. Methanol density, divided by velocity gradient, for all models is $0.67 \times 10^{-2} \text{ cm}^{-3}/(\text{km s}^{-1}/\text{pc})$.

Model	T_{kin} (K)	n_{H_2}	44/95 GHz intensity ratio
1	20	0.56E+5	3.3
2	50	0.56E+5	1.7
3	100	0.56E+5	0.4
4	20	0.56E+6	1.2

$7_1 A^+$ transition is 18.5 K above the upper level of the 44-GHz $7_0 - 6_1 A^+$ transition. Therefore the population of the former is expected to be lower than the population of the latter, resulting in the lower intensity of 95-GHz emission compared to the intensity of the 44-GHz transition, although it is difficult to estimate the difference without any knowledge of the kinetic temperature and particle density in the source.

We used LVG code to calculate the intensity ratios of the $7_0 - 6_1 A^+$ and $8_0 - 7_1 A^+$ transitions in a collisional excitation model for four different parameter sets. The model parameters and the intensity ratios are presented in Table 6. The collisional selection rules are based on the paper by Lees & Haque (1974) and imply that $\Delta K = 0$ collisions are preferred by a factor of four. For model 1 with a gas temperature 20 K and density $0.56 \times 10^5 \text{ cm}^{-3}$, the ratio of the 44- and 95-GHz intensities is 3.3, i.e., close to the mean observed ratio. The 95 GHz intensity is lower due to the lower population of the $8_0 A^+$ level relative to that of the $7_0 A^+$ level and due to a weaker inversion at 95 GHz. Increasing either the gas temperature or the density decreased the model ratio below the observed value. Thus, our results favour class I maser model with gas temperature about 20 K and density less than 10^6 cm^{-3} .

5 SUMMARY

1. As a result of a survey in the southern hemisphere 85 methanol emission sources were detected in the $8_0 - 7_1 A^+$ transition at 95 GHz. This survey together with a similar Onsala survey (Val'tts et al. 1995) completes a whole sky survey of methanol emission at 95 GHz.

2. Most of the detected sources are class I methanol masers, and the majority of them have counterparts in other class I methanol transitions, such as the $7_0 - 6_1 A^+$ at 44 GHz.

3. The previously found correlation between the methanol maser emission intensity at 44 and 95 GHz is confirmed here, using a larger sample of sources.

4. A maser model with collisional excitation based on LVG calculations can explain the observed intensity ratio at 44 and 95 GHz and gives constraints on the temperature and particle density.

6 ACKNOWLEDGEMENTS

I.E.V. is grateful to the ATNF for the hospitality, and to the staff of Mopra observatory for the help with the ob-

servations. The Australia Telescope is funded by the Commonwealth of Australia for operation as a National Facility managed by CSIRO. Travel to Australia for I.E.V. was aided by grant 96/1990 from the Australian Department of Industry, Science and Tourism. The work of I.E.V., V.I.S., S.V.K. and G.M.L. was partly supported by the grants 95-02-05826 and 98-02-16916 from the Russian Foundation for Basic Research and by the Federal Program "Astronomiya" (Project N 1.3.4.2). S.P.E thanks the Queen's trust for the computing system used to process the data from these observations. The authors would like to thank Ms V. Oakley and Mr J. Saab for their assistance during the observations and initial data processing.

REFERENCES

Bachiller R., Menten K.M., Gómez-González J., Barcia A., 1990, A&A, 240, 116
 Brand J., Blitz L., 1993, A&A, 275, 67
 Caswell J.L., Vaile R.A., Ellingsen S.P., Whiteoak J.B., Norris R.P., 1995a, MNRAS, 272, 96
 Cragg D.M., Johns K.P., Godfrey P.D., Brown R.D., 1992, MNRAS, 259, 203
 De Lucia F.C., Herbst E., Anderson T., Helminger P., 1989, J. Mol. Spectr., 134, 395
 Ellingsen S.P., von Bibra M.L., McCulloch P.M., Norris R.P., Deshpande A.A., Phillips C.J., 1996, MNRAS, 280, 378
 Ellingsen S.P., Otrupcek R., Legge D.R., McCulloch P.M., Norris R.P., 1999, MNRAS, in preparation
 Genzel R., Stutzki J., 1989, ARA&A, 27, 41
 Haschick A.D., Menten K.M., Baan W.A., 1990, ApJ, 354, 556
 Houghton S., Whiteoak J.B., 1995, MNRAS, 273, 1033
 Kalenskii S.V., Bachiller R., Berulis I.I., Val'tts I.E., Gómez-González J., Martin-Pintado J., Rodriguez-Franco A., Slysh V.I., 1992, AZh 69, 1002
 Kalenskii S.V., Liljestrom T., Val'tts I.E., Vasil'kov V.I., Slysh V.I., Urpo S., 1994, A&AS, 103, 129
 Kogan L., Slysh V.I., 1998, ApJ, 497, 800
 Kutner M.L., Ulich B.L., 1981, ApJ, 250, 341
 Lees R.M., Haque S.S., 1974, Can. Journ. of Phys., 52, 2250
 Menten K.M., in "Skylines", Proceedings of the Third Haystack Observatory Conference on Atoms, Ions and Molecules. Eds. Haschick A.D. & Ho P.T.P., Astronomical Society of the Pacific Conference Series, 1991, 119
 Morimoto M., Ohishi M., Kanagawa T., ApJ, 1985, 288, L11
 Neckel T., 1978, A&A, 69, 51
 Norris R.P., Whiteoak J.B., Caswell J.L., Wieringa M.H., Gough R.G., 1993, ApJ, 412, 222
 Plambeck R.L., Menten K.M., 1990, ApJ, 364, 555
 Pratap P., Menten K.M., 1992, In: Astrophysical Masers, eds Clegg and Nedoluha, Springer Verlag, Berlin, Lecture Notes in Physics, 412, 211
 Slysh V.I., Kalenskii S.V., Val'tts I.E., Otrupcek R., 1994, MNRAS, 268, 464
 Slysh V.I., Val'tts I.E., Kalenskii S.V., Golubev V.V., 1999, ARep, 43, 785
 Sung H., Bessell M.S., Lee S., 1997, AJ, 114, 2644
 Thronson H.A. Jr, Lowenstein R.F., Stokes G.M., 1979, AJ, 84, 1328
 Val'tts I.E., 1998, AstL, 24, 788
 Val'tts I.E., 1999a, ARep, 43, 157
 Val'tts I.E., 1999b, ARep, 43, 148
 Val'tts I.E., Dzura A.M., Kalenskii S.V., Slysh V.I., Booth R.S., Winnberg A., 1995, AZh, 72, 22
 Val'tts I.E., Ellingsen S.P., Slysh V.I., Kalenskii S.V., Otrupcek R., Voronkov M.A., 1999, MNRAS, 310, 1077

